J. Fluid Mech. (1997), *vol.* 332, *pp.* 215–245

Convection and flow in porous media. Part 1. Visualization by magnetic resonance imaging

By M. D. SHATTUCK[1], R. P. BEHRINGER[1], G. A. JOHNSON[2] AND J. G. GEORGIADIS[3]

[1]Department of Physics and Center for Nonlinear and Complex Systems, Duke University, Durham NC, 27708-0305, USA

[2]Center for In-Vivo Microscopy, Duke University Medical Center, Durham, NC 27710, USA

[3]Department of Mechanical and Industrial Engineering, University of Illinois at Urbana-Champaign, Urbana, IL 61801, USA

(Received 21 March 1996 and in revised form 9 July 1996)

We describe an experimental study of porous media convection (PMC) from onset to $8Ra_c$. The goal of this work is to provide non-invasive imaging and high-precision heat transport measurements to test theories of convection in PMC. We obtain velocity information and visualize the convection patterns using magnetic resonance imaging (MRI). We study both ordered and disordered packings of mono-disperse spheres of diameter $d = 3.204 \pm 0.029$ mm, in circular, rectangular, and hexagonal planforms. In general, the structure of the medium plays a role which is not predicted by theories which assume a homogeneous system. Disordered media are prepared by pouring mono-disperse spheres into the container. Large ordered regions of close packing for the spheres, with grain boundaries and isolated defects, characterize these media. The defects and grain boundaries play an important role in pattern formation in disordered media. Any deviation from close packing produces a region of larger porosity, hence locally larger permeability. The result is spatial variations in the Rayleigh number, Ra. We define the critical Ra, Ra_c, as the Rayleigh number at the onset of convection in the ordered regions. We find that stable localized convective regions exist around grain boundaries and defects at $Ra < Ra_c$. These remain as pinning sites for the convection patterns in the ordered regions as Ra increases above Ra_c up to $5Ra_c$, the highest Ra studied in the disordered media. In ordered media, spheres are packed such that the only deviations from close packing occur within a thin ($<d$) region near the vertical walls. Stable localized convection begins at $0.5Ra_c$ in the wall regions but appears to play only a weak role in the pattern formation of the interior regions (bulk), since different stable patterns are observed in the bulk at the same Ra after each cycling of Ra below Ra_c, even for similar patterns of small rolls in the wall regions. The experiments provide a test of the following predictions for PMC: (i) that straight parallel rolls should be linearly stable for $Ra_c < Ra < 5Ra_c$; (ii) that at onset, the rolls should have a dimensionless wavevector $q_c = \pi$; (iii) that at the upper end of this range rolls should lose stability to cross-rolls; (iv) that the initial slope of the Nusselt curve should be 2; (v) that there should be a rapid decay of vertical vorticity – hence no complex flows, such as those which occur for Rayleigh–Bénard convection (RBC) within the nominal regime of stable parallel rolls. These predictions are in partial agreement with our findings for the bulk convection in the ordered media. We observe roll-like structures which relax rapidly to stable patterns between Ra_c and $5Ra_c$. However we find a wavenumber which is 0.7π compared to π derived from linear stability theory. We find an asymmetry between the size of

the upflowing regions and downflowing regions as Ra grows above Ra_c. The ratio of the volume of the upflowing to the volume of the downflowing regions decreases as Ra increases and leads to a novel time-dependent state, which does not consist of cross-rolls. This time-dependent state begins at $6Ra_c$ and is observed up to $8Ra_c$, the largest Ra which we studied. It seems likely that the occurrence of this state is linked to departures from the Boussinesq approximation at higher Ra. We also find that the slope of the Nusselt curve is 0.7, which does not agree with the predicted value of 2.

1. Introduction

Buoyancy-driven porous media convection, PMC, and porous media flows in general are of significant technical importance, with applications in insulation, groundwater filtration, oil and gas recovery and many industrial processes. Combarnous & Bories (1975) discusses these and other applications.

PMC is also interesting as a nonlinear pattern forming system. Such systems, including the bulk fluid analogue to PMC, Rayleigh–Bénard convection (RBC) are of increasing interest. Recent advances (Behringer 1985; Cross & Hohenberg 1993) in understanding pattern formation in RBC are due in large part to its amenability to theoretical analysis and to the ease of visualization with the shadowgraph technique (Busse & Whitehead 1971; Rasenat *et al.* 1989; deBruyn *et al.* 1996).

The conventional equations of motion for PMC (Horton & Rodgers 1945, Lapwood 1948), are simpler than those of RBC but still predict a number of the same features, including an initial instability with a non-zero wavenumber, nonlinear pattern selection, and some common secondary instabilities. Conventional models of PMC also differ from RBC in a number of ways. For instance, the momentum equation for PMC is linear; in the complete theoretical description, the only nonlinearity comes from the coupling of the velocity and temperature fields in the heat equation. In PMC, the vertical vorticity decays away quickly, which provides an interesting test of the importance of vertical vorticity to the complex dynamics observed for low to moderate Prandtl number fluids in RBC (Morris *et al.* 1993; Xi, Gunton & Vinals 1993).

Our understanding of PMC has lagged that of RBC, especially in experiments. This is due primarily to the fact that PMC is very difficult to visualize, since light is typically dispersed or absorbed by the solid matrix in porous media. Until recently, there have been no effective PMC visualization techniques which determine the convection pattern non-invasively. The current lack of and need for visualization and local velocity information has been pointed out in recent reviews by Torrance *et al.* (1982) and by Georgiadis (1991). Much of the existing experimental data are limited to heat transfer measurements (Schneider 1963; Katto & Masuoka 1967; Combarnous 1970; Buretta & Berman 1976; Kaneko, Mohtadi & Aziz 1974; Yen 1974), and these data are often inconsistent with each other, a fact which the present studies, and related work (Howle, Behringer & Georgiadis 1997) may explain. Specifically, the convective pattern, which can significantly affect the heat transport, is sensitive to the structure of the medium.

PMC visualization techniques in the past have been typically either invasive, or limited to special geometries or to a few points. In general, there has been no quantitative velocity information. For example, Elder (1967) visualized Hele-Shaw convection to gain qualitative information about PMC based on the correspondence

between Hele-Shaw equations and PMC equations. Prasad, Kulacki & Keyhani (1985) used point measurement techniques by inserting thermocouples into a convection cell to map the temperature. Bories & Thirriot (1969) observed PMC with a free upper surface using aluminium particles sprinkled on a thin layer of fluid above the medium. Beckermann, Viskanta & Ramadhyani (1988) studied a convective system with vertical layers of porous media and clear fluid. They visualized the temperature patterns in the bulk fluid and used that information to infer the pattern in the porous region. Lister (1990) visualized convection by looking in from above through a thin Teflon sheet with stainless steel mesh underneath. The mesh helped maintain isothermal boundary conditions and served as the cathode in an electrolysis process involving thirteen graphite slabs buried in the medium. Visualization was accomplished by a pH indicator in the fluid which changed colour near the graphite and was then carried to the top of the cell by the convection. However, the graphite plates provided spatial perturbations, and the fluid was a mixture rather than a pure fluid. Lein & Tankin (1992) used a technique based on the Christiansen filter concept to visualize temperature profiles in two-dimensional PMC. This non-invasive technique works well for this geometry, but it cannot be used to determine flow patterns in general three-dimensional media. Recently, however, Howle, Behringer & Georgiadis (1993*a,b*) used a modified shadowgraph technique to visualize PMC with special solid matrices that have all surfaces either parallel or perpendicular to the incoming light rays. While this technique is non-invasive, it does not work for an arbitrary medium and does not provide velocity information.

To our knowledge, this work presents the first quantitative velocity profiles in PMC obtained while maintaining close to ideal conditions for a packed bed of spheres. By using magnetic resonance imaging (MRI) we measure the local density, velocity, and temperature of a flowing fluid, such as water. In the following sections we discuss the theory of PMC (§ 2), the apparatus and MRI technique used for these measurements (§ 3), and the results for various planforms and packing arrangement (§ 4). We also include results for pressure-driven flows (Georgiadis *et al.* 1991) which provide a test of the MRI technique (Givler & Altobelli 1994; Kutsovsky *et al.* 1996; Lebon *et al.* 1996) in another setting. Brief accounts of this work have appeared elsewhere Shattuck *et al.* (1994, 1995).

2. Theory

2.1. *Equations of motion for PMC*

The equations of motion for porous media are based on an empirical relation between the pressure applied across a uniform porous medium and the bulk flow rate through the medium (Darcy 1856). This relation is expressed by Darcy's law,

$$v_x = -\frac{\gamma}{\eta}\frac{\partial P}{\partial x}, \tag{2.1}$$

where v_x is the fluid velocity averaged over the area perpendicular to the flow direction, x, η is the fluid dynamic viscosity, P is the pressure; γ is a geometrical property of the porous medium called the permeability. Ergun (1952) determined an empirical relation between γ, d, the pore size, and ϕ, the porosity or void fraction for spherical particles. Ergun's relation,

$$\gamma = \frac{d^2\phi^3}{150(1-\phi)^2}, \tag{2.2}$$

can also be derived from Carman-Kozeny's hydraulic radius theory; in this case, the constant is 180 instead of 150. Either of these gives a reasonable estimate of γ. While (2.1) is one-dimensional, the three-dimensional generalization (Nield & Bejan 1992; Bear 1988) is

$$\boldsymbol{v} = \eta^{-1}\boldsymbol{\gamma} \cdot \nabla P, \tag{2.3}$$

where $\boldsymbol{\gamma}$ is a second rank tensor. In the case of an isotropic media (2.3) reduces to

$$\nabla P = -\frac{\eta}{\gamma}\boldsymbol{v}. \tag{2.4}$$

In this case, γ is a scalar. Equation (2.4) has been investigated both experimentally and theoretically for small $\boldsymbol{v}$, such as those that occur in PMC (Dullien 1979; Whitaker 1986; Ene & Poliševski 1987).

PMC, which was first described theoretically by Horton & Rodgers (1945) and Lapwood (1948), consists of a fluid-saturated medium with uniform height, H, in the z-direction. In the conventional scenario, the system is homogeneous and isotropic. The temperature is specified on the isothermal horizontal boundaries, $T(z = -H/2) = T_1$ and $T(z = +H/2) = T_2$. From T_1 and T_2, we define a reference temperature $T_0 = (T_1 + T_2)/2$ and a temperature difference, $\Delta T = (T_2 - T_1)/2$. In the case of convection, there is a buoyant force on the fluid which must be added to Darcy's law (2.4), and we also include an acceleration term (Nield & Bejan 1992), which gives

$$\rho_0 a \frac{\partial \boldsymbol{v}}{\partial t} = -\nabla P - \frac{\eta}{\gamma}\boldsymbol{v} - \rho_f g\hat{\boldsymbol{z}} \tag{2.5}$$

as the momentum equation, where g is the acceleration due to gravity, and a is a medium-dependent acceleration coefficient. In (2.5), we have used the Oberbeck–Boussinesq approximation (Oberbeck 1979; Boussinesq 1903), in which all fluid parameters are assumed independent of T and P, except in the buoyancy term:

$$\rho_f = \rho_0(1 - \alpha(T - T_0)).$$

Here, α is the coefficient of thermal expansion. The equation for mass conservation is

$$\nabla \cdot \boldsymbol{v} = 0 \tag{2.6}$$

for an incompressible fluid saturating a uniform porous medium. The temperature varies according to the heat equation,

$$(\rho c)_m \frac{\partial T}{\partial t} + (\rho c_P)_f \boldsymbol{v} \cdot \nabla T = k_m \nabla^2 T, \tag{2.7}$$

where c is the specific heat, k is the thermal conductivity and the subscripts m and f refer respectively to properties of the porous medium and fluid combined and to properties of the fluid alone. We define the effective thermal diffusivity by

$$\kappa_m = \frac{k_m}{(\rho c_P)_f}. \tag{2.8}$$

The boundary conditions for $\boldsymbol{v}$ are no flux, which imply for the horizontal boundaries that $v_z(z = \pm H/2) = 0$; the boundary conditions on T are given above. In this model, slip is allowed at the boundaries, which suggests that the sidewalls may play a weaker role in pattern selection for PMC than for RBC.

A simple solution to (2.5), (2.6), and (2.7) is

$$\boldsymbol{v} = 0, \tag{2.9}$$

$$T = T_0 - \frac{\Delta T}{H} z, \tag{2.10}$$

$$P = P_0 + \rho_0 g \left(z + \frac{\alpha}{2H} z^2 \right), \tag{2.11}$$

where P_0 is pressure at $z = 0$. This solution corresponds to pure heat conduction through the layer, with the fluid stationary, and is called the conduction solution. We will non-dimensionalize (2.5), (2.6), and (2.7) using this solution and H, $(\sigma H^2)/\kappa_m$, κ_m/H, and $\Delta T/Ra$ as the scale for length, time, velocity, and temperature respectively. We also introduce the dimensionless convective temperature field, θ:

$$\theta = \frac{Ra}{\Delta T}(T - (T_0 - \Delta T z)). \tag{2.12}$$

The non-dimensional equations become,

$$\frac{A}{\mathrm{Pr}} \frac{\partial \boldsymbol{u}}{\partial t} = -\nabla P - \boldsymbol{u} + \theta \hat{\boldsymbol{z}} \tag{2.13}$$

$$\frac{\partial \theta}{\partial t} + \boldsymbol{u} \cdot (\nabla \theta - Ra \hat{\boldsymbol{z}}) = \nabla^2 \theta \tag{2.14}$$

$$\nabla \cdot \boldsymbol{u} = 0, \tag{2.15}$$

where

$$Ra = \alpha \gamma H g \Delta T / \nu \kappa_m, \tag{2.16}$$

$$Pr = \nu / \kappa_m, \tag{2.17}$$

$$Da = \gamma / H^2, \tag{2.18}$$

$$A = aDa/\sigma, \tag{2.19}$$

$$\sigma = (\rho c)_m / (\rho c_P)_f. \tag{2.20}$$

P has also been modified to absorb any terms which can be written as gradients. Our choice of temperature scale is different from some scalings in the PMC literature, and is chosen, for comparison, to correspond to conventional usage in the RBC literature.

When the Rayleigh number Ra is below a critical value, Ra_c, the fluid is stationary, but when $Ra > Ra_c$ it begins to move. The Prandtl number Pr and A determine the relative importance of the acceleration term, and Da is the Darcy number. Da is typically a small number (in our experiment $Da = 2 \times 10^{-5}$ based on (2.2)) and the acceleration term is often neglected. The time scale

$$\tau_v = (\sigma H^2)/\kappa_m, \tag{2.21}$$

or vertical thermal diffusion time, is a measure of the relevant time for thermal changes to propagate from the bottom to the top of the cell containing the porous medium. The horizontal diffusion time is $\tau_h = \Gamma^2 \tau_v$, where Γ is the aspect ratio. Γ is defined as L/H, where L is a typical lateral dimension of the cell. While Γ does not play a role in the theory discussed below, which considers only horizontally infinite systems, it is important in physical experiments. For instance, in RBC the lateral boundaries are known to play a fundamentally important role in pattern selection, even for relatively large Γ. For PMC, there is relatively little information on the effects of the lateral boundaries on pattern selection, and the present study takes a first step in addressing this issue.

2.2. *Linear stability*

Lapwood (1948) applied stability analysis to (2.13) to (2.15), and found that the conduction state loses linear stability to a disturbance of wavenumber, $q_c = \pi = 2\pi/\lambda$, at a critical temperature corresponding to $Ra_c = 4\pi^2$. The value for Ra_c was verified by several experiments (Combarnous 1975; Close, Symons & White 1985, for example). The bifurcation parameter for convection is then the reduced Rayleigh number,

$$\epsilon = \frac{Ra - Ra_c}{Ra_c}. \tag{2.22}$$

While linear analysis can predict the wavelength of the rolls at onset, it has limitations. For instance, it cannot predict nonlinear three-dimensional patterns.

2.3. *Limits on the Darcy number*

We consider next the constraints involving the Darcy number, relaxation times, and the extent to which the Boussinesq approximation is satisfied. In an ideal experiment, Da should be infinitesimally small, non-Boussinesq effects should be negligible, and relaxation times should be short. These three conditions are mutually conflicting, however. If we want to restrict fluid property variation so that the Boussinesq approximation is valid, we must impose a limit on ΔT. A reasonable choice for the fluid used in these experiments might be a maximum of $\Delta T = 10$ K at the onset of convection. For fixed ΔT, and $Ra \simeq Ra_c$, the definition of the porous Rayleigh number (equation (2.16)) and the the Ergun correlation for permeability

$$\gamma = \frac{d^2\phi^3}{150(1-\phi)^2}, \tag{2.23}$$

imply that the layer height, H, and the bead diameter of a packed spherical bead bed, d, are restrained by the curve

$$d^2H = \frac{6 \times 10^3 \kappa v\,(1-\phi)^2}{\alpha g \Delta T \phi^3}. \tag{2.24}$$

For matrices which are not constructed from sphere packings, we still expect this constraint to apply semiquantitatively, with d representing a typical pore size. For $\Delta T = 10$ K, for a typical porosity for beds of packed spheres, $\phi = 0.4$, and for fluid properties corresponding to water at 20°C, equation (2.24) gives the solid curve in figure 1. ΔT smaller than 10 K are to the right of this curve. We are also restrained to the left of the $d = H$ line (dashed line in figure 1): i.e. to have a porous medium, the pore scale can be no larger than the height. A spatially homogeneous medium, should satisfy $H/d \gg 1$ however, or alternatively, $Da \ll 1$. If we choose $Da = 2 \times 10^{-5}$ as an upper limit, a relatively large Darcy number, then the condition

$$H = d\left(\frac{150Da\,(1-\phi)^2}{\phi^3}\right)^{-1/2} \tag{2.25}$$

yields the dotted line in figure 1. We must keep to the left of this line. The third experimental condition, that of tractable relaxation times, imposes the final contraint. Except near the point of convective onset where the relaxation times diverge, the characteristic time for vertical thermal diffusion across the layer is $\tau_v \equiv H^2/\kappa_m$. This leads to a height restriction: if the layer is too tall, relaxation times become so

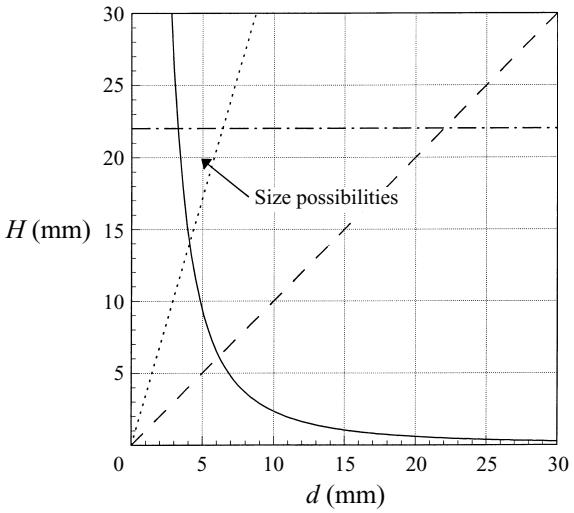

FIGURE 1. Acceptable experimental pore sizes, d, and layer heights, H.

long that meaningful experiments under steady conditions become impossible. A maximum tolerable relaxation time sets a maximum height H:

$$H = (\kappa\tau_v)^{\frac{1}{2}}. \tag{2.26}$$

Given these contraints, the area of possible experimental parameters is quite small, i.e. for random sphere packings the small triangular region in figure 1 indicated by the arrow. The important point is that H/d cannot, in general, be chosen so large that the medium is effectively homogeneous on the scale of $\lambda = 2\pi/q$.

For example, in the case of water at 40 °C, 3.175 mm plastic beads with $H = 1$ cm, $\Delta T_c = 10$ K. Decreasing the bead diameter to 1 mm increases ΔT_c to greater than 100 K. However, the alternative, making H larger is equally problematic, since $\tau_v \propto H^2$ cannot be too large or only transients will be observed. For the example above with $H = 1$ cm, $\tau_v = 16$ min and the horizontal diffusion time, $\tau_h = \Gamma^2\tau_v$, is 26 hours for $\Gamma = 10$. An increase of H by a factor of 3 at fixed bead diameter and Γ in order to obtain a comparable reduction in δ/H would result in relaxation times of $\tau_v = 27$ hours and $\tau_h = 3.6$ months, which are clearly unacceptable. To obtain acceptable relaxation times only $d/H < 1$ can be realized.

2.4. *Comparison of PMC and RBC near onset*

Although PMC and RBC are qualitatively similar in a number of respects, there are also important differences. Here, we contrast these two systems.

2.4.1. *Similarities between PMC and RBC*

Above, but near the threshold of, a nonlinear instability it is possible to derive amplitude equations, which describe the large-scale envelope of a basic roll-like state (Newell & Whitehead 1969; Segel 1969; Newell, Passot & Lega 1993). In this regime, the bifurcation parameter, ϵ, is small and provides the basis for a multiple-scales perturbation method leading to a small number of amplitude equations describing the universal behaviour of large classes of systems. PMC, viewed as a homogeneous system, and RBC belong to the class I_s Cross & Hohenberg 1993 systems as defined by linear stability analysis. Class I_s, or stationary periodic, includes any nonlinear system

which loses stability of a uniform state to a time-independent non-zero-wavelength pattern. For a base state of straight parallel rolls, the form of the amplitude equation for all isotropic systems with a type I_s instability is the same:

$$\tau_0 \frac{\partial A}{\partial t} = \epsilon A + \xi_0^2 \left[\frac{\partial}{\partial x} - \left(\frac{\mathrm{i}}{2q_c} \right) \frac{\partial^2}{\partial y^2} \right]^2 A - g_0 |A|^2 A. \tag{2.27}$$

Here, τ_0, ξ_0, and g_0 are the scales for time, space, and amplitude, respectively; q_c is the wavenumber at onset, defined above, and $A(x, y, t)$ is a complex amplitude which depends on space and time. Near onset, all the variation among different members of this class comes through the parameters τ_0, ξ_0, q_c, and g_0. In the case of PMC and RBC the amplitude and the basic state defined by the wavenumber determine the velocity and the temperature field as

$$U(x, y, z, t) = U_o(z)[A(x, y, t) \exp(\mathrm{i}q_c x) + A^*(x, y, t) \exp(-\mathrm{i}q_c x)] + O(\epsilon), \tag{2.28}$$

where U can be a component of the velocity in any direction or the temperature, and U_0 is determined from linear analysis. For concreteness we have assumed that the base state is parallel rolls in the $\hat{\boldsymbol{x}}$-direction. For PMC, τ_0 and ξ_0, can be derived from linear stability analysis (Joseph 1976; Shattuck 1995):

$$\tau_0 = \frac{1 + 2\pi^2 A/Pr}{2\pi^2} = \frac{1 + 19.739\, A/Pr}{19.739} \tag{2.29}$$

and

$$\xi_0 = \frac{1}{\pi} = 0.3183. \tag{2.30}$$

Typically, we expect that A/Pr is so small that it can be ignored, in which case, $\tau_0 = (2\pi^2)^{-1}$. The parameter g_0 determines the scale of A, as discussed in the context of the Nusselt number in §2.7.

For RBC, the time scale and length scale in the RBC amplitude equations are

$$\tau_0 = \frac{1 + 0.5117 Pr^{-1}}{19.65} \tag{2.31}$$

and

$$\xi_0 = 0.3847. \tag{2.32}$$

The scales τ_0 and ξ_0 have the same qualitative form for both RBC and PMC. Since A is likely to be very small, the coefficients for PMC are more like those for RBC when Pr is large. To the extent that the amplitude equation applies, we would expect qualitatively similar behaviour for both PMC and RBC near onset.

2.4.2. *Differences between PMC and RBC*

One of the key differences between PMC and RBC lies in the momentum equation (see (2.13)), which for RBC in dimensionless form is

$$\frac{1}{Pr} \left(\frac{\partial \boldsymbol{u}}{\partial t} + \boldsymbol{u} \cdot \nabla \boldsymbol{u} \right) = -\nabla P - \nabla^2 \boldsymbol{u} + \theta \hat{z}. \tag{2.33}$$

Unlike the porous case, this equation is nonlinear and also of higher order. By contrast, the forms of the heat equations and continuity equations for the two systems are the same. The Rayleigh numbers for PMC and RBC are related by $Ra^{\mathrm{rbc}} = RaDa^{-1}$.

Also different between PMC and RBC is the appropriate set of boundary conditions. For PMC, the accepted boundary condition on the velocity, assuming (2.13), is

one of no flux, whereas the corresponding conditions for RBC in the case of physical experiments are no flux and no slip. This difference in boundary conditions also reflects the difference in the order of the respective momentum equations.

The last important difference between these two convective systems concerns the vertical vorticity. From the vertical component of the curl of (2.13) we obtain

$$\frac{\partial \xi_z}{\partial t} = -\frac{Pr}{A}\xi_z, \tag{2.34}$$

where the vertical vorticity, $\xi_z = (\nabla \times \boldsymbol{u})\cdot\hat{\boldsymbol{z}}$. The solution to (2.34) for an initial value, ξ_0, is

$$\xi_z = \xi_0 \exp\left(-\frac{Pr}{A}t\right). \tag{2.35}$$

Thus, the vertical vorticity decays with a non-dimensional time constant,

$$\tau_\xi = \frac{A}{Pr}. \tag{2.36}$$

Using the time scale defined above we see that the dimensional time constant is

$$\tau_\xi = \frac{A\sigma H^2}{\kappa_m Pr} = \frac{a\gamma}{v} = 4.5\times10^{-3}a \text{ s}. \tag{2.37}$$

Assuming that a is of order one, the vorticity decays on millisecond time scales. From (2.33) it is clear that for RBC, the equation for the vertical vorticity is a complicated nonlinear equation. There is some evidence (Siggia & Zippelius 1981; Morris *et al.* 1993; Xi *et al.* 1993) that vertical vorticity is responsible for complicated behaviour such as spiral chaos in moderate Prandtl number RBC (Greenside, Cross & Coughran 1988; Greenside 1995, personal communication). If vertical vorticity is essential for spiral chaos or other complicated behaviour, then such behaviour should be absent in PMC. Thus, we would expect that PMC will yield steady roll-like patterns within the predicted linear stability region.

2.5. *Symmetry*

Equations (2.13) to (2.15) are invariant under the following transformation:

$$\begin{aligned} z &\to -z \\ u_z &\to -u_z \\ \theta &\to -\theta. \end{aligned}$$

This symmetry is important in determining the pattern near onset. In particular, the pattern should consist of rolls of equal width, and the amplitude A should have the symmetry $A \to -A$. In §2.4.1, we described the amplitude equations for the base state of straight parallel rolls. Amplitude equations can also be derived for a base state consisting of the superposition of multiple straight rolls Newell & Whitehead 1969. Of particular interest is the case where three roll directions co-exist at 60° angles to each other. In this state, the base pattern is hexagonal. When the symmetry $A \to -A$ is present, the roll state is stable. However, if the symmetry is broken, then a quadratic term appears in the amplitude equations for the hexagonal state, which can be stable (Busse 1967; Bodenschatz *et al.* 1991). For RBC, Busse (1967) has shown theoretically, and Bodenschatz *et al.* (1991) have shown experimentally that hexagons are typically stable in only a small range near Ra_c, depending on a parameter P which quantifies departures form the Oberbeck–Boussinesq approximation. Comparable quantitative

theories do not exist for PMC, at least to our knowledge. However, we expect that qualitatively similar behaviour should occur for the PMC case.

The symmetry in (2.13) to (2.15) depends on several assumptions. First, the boundary conditions on u and θ must be symmetric in the $\hat{z}$-direction. Second, the Boussinesq approximation must hold: i.e. the fluid parameters, with the exception of the density, must have negligible dependence on the temperature. Third, for porous media, there is the additional condition that the pore structure not depend on the vertical direction.

2.6. *Nonlinear analysis and convection patterns above onset*

Weakly nonlinear analysis predicts two-dimensional roll states near onset for systems with vertical mid-plane symmetry (Busse 1985; Newell & Whitehead 1969; Newell *et al.* 1993). But, in most PMC experiments, when the pattern was determined, it was found to be hexagonal or polygonal (Bories & Thirriot 1969; Lister 1990). An exception is Howle *et al.* (1993*a,b*, 1997), who have obtained straight parallel rolls in some cases, and polygonal patterns in other media, depending on the structure of the medium. Bories & Thirriot (1969) and Nield & Bejan (1992) attribute polygonal patterns to broken symmetry in the boundary conditions. Recently, however, Zimmermann, Sesselberg & Petruccione (1993) have provided an alternative explanation which is consistent with the present work and that of Howle *et al.* They have shown that localized patterns can result if *Ra* varies randomly in the horizontal plane of the convection layer, a situation which can occur easily for PMC.

Further stability analysis has been done to determine secondary instabilities (Straus 1974; Busse & Joseph 1972) of two-dimensional rolls to three-dimensional disturbances. Straus (1974) predicts that two-dimensional rolls lose stability to a cross-roll state at $\epsilon = 5$. However, we are unaware of a direct test of these calculations.

2.7. *Heat transport*

The Nusselt number, *Nu*, is a non-dimensional measure of heat transport of the medium. This quantity is easily measured and provides several important checks on theory. *Nu* is the ratio of the effective thermal conductivity, k_{eff}, of the medium to the true thermal conductivity of the medium below onset, k_m:

$$Nu = \frac{k_{eff}}{k_m}. \tag{2.38}$$

$Nu = 1$ below the onset of convection, and typically increases uniformly with increasing ϵ above the onset of convection, at least until there is a significant change in the convective pattern. In the ideal case, there is a discontinuity in the slope of *Nu* at onset which provides an easy way to determine ΔT_c, the critical temperature difference for the onset of convection. The Nusselt number is also simply related to the spatial average of the product of the vertical velocity and the temperature perturbation, θ. $Nu(\epsilon)$ provides an important link with theory (Busse & Joseph 1972; Gupta & Joseph 1973; Palm, Weber & Kvernvold 1972), since the parameter g_0 for homogeneous isotropic PMC is predicted to be such that for small positive ϵ,

$$Nu = 1 + 2\epsilon. \tag{2.39}$$

3. Techniques and apparatus

3.1. *Velocity measurements with MRI*

MRI is a non-invasive technique based on nuclear magnetic resonance (NMR), which measures relaxation-weighted proton density and can also yield fluid velocity and temperature. There are several techniques for measuring flow with MRI: time of flight (Singer 1980), phase contrast (Odonnell 1985; Dumoulin 1986), and phase encoding. We use phase encoding exclusively, which provides information about velocity distribution, temperature, and density. The theory which we present here was developed by Moran (1982); the first experimental images were produced by Redpath *et al.* (1984). In addition, several recent experiments have exploited MRI to obtain information on pressure-driven flows (Georgiadis *et al.* 1991; Givler & Altobelli 1994; Kutsovsky *et al.* 1996; Lebon *et al.* 1996).

We have used an Oxford 2 T magnet, with GE 18 G cm^{-1}, shielded, 15.2 cm diameter bore gradient coils, controlled by a GE Omega console. An 85.5 MHz tunable radio frequency coil was produced using etched copper-clad mylar.

Although a full treatment of NMR Slichter 1978 or MRI Callaghan 1991 requires quantum mechanics, a semi-classical approach suffices to understand the basics of MRI. The nucleus of an atom may be thought of classically as a spinning charge distribution with a magnetic moment vector, $\boldsymbol{m}$, and an angular momentum vector, $\boldsymbol{L}$. The Bloch equation describes the dynamics of $\boldsymbol{m}$ for a nucleus in an externally applied magnetic field, $\boldsymbol{H}$ (Bloch 1946):

$$\frac{\mathrm{d}\boldsymbol{m}}{\mathrm{d}t} = \boldsymbol{m} \times \gamma_g \boldsymbol{H}. \tag{3.1}$$

Here, γ_g is the gyromagnetic ratio for the given nucleus. Equation (3.1) is the same classically or quantum mechanically, although γ_g is different for the two cases, and $\boldsymbol{m}$ is the expected value of the magnetic moment operator in the full quantum treatment.

According to (3.1), for a magnetic field, $\boldsymbol{H}$, with a fixed direction, $\boldsymbol{m}$ precesses about $\boldsymbol{H}$ at an instantaneous rotation rate, ω, given by the Larmor equation:

$$\omega = \gamma_g |\boldsymbol{H}|. \tag{3.2}$$

If $\boldsymbol{H} = \boldsymbol{H}_0 \hat{\boldsymbol{z}}$, then $\omega_L = \gamma_g \boldsymbol{H}_0$ where ω_L is the Larmor frequency. In the present experiments, $\boldsymbol{H}_0 = 2$ T. For hydrogen atoms in water molecules, the Larmor frequency is in the radio frequency (r.f.) range: $\omega_L = 85.5$ MHz. Because the spins precess at ω_L, it is often convenient to use a frame which also rotates at ω_L.

In the presence of a second time-varying magnetic field, $\boldsymbol{H}_1 = \boldsymbol{H}_1(\cos(\omega_L t)\hat{\boldsymbol{x}} + \sin(\omega_L t)\hat{\boldsymbol{y}})$, $\boldsymbol{m}$ precesses about $\boldsymbol{H}_1$. In a frame rotating at ω_L(the 'rotating frame'), this field transforms to $\boldsymbol{H}_1 \hat{\boldsymbol{x}}$. Over a short time, τ, $\boldsymbol{m}$ rotates by an angle, $\alpha = \gamma_g \boldsymbol{H}_1 \tau$, about the direction of $\boldsymbol{H}_1$ ($\hat{\boldsymbol{x}}$ in this case) in the rotating frame. The application of such a field is called an α-pulse in the x-direction. This process is a resonance phenomenon, so the r.f. field must be at the Larmor frequency to change the angle.

For a large collection of spins in a localized region of space, $\mathrm{d}V$, we define the magnetization or density of dipole moments, $\boldsymbol{M}$, and the total magnetization,

$$\boldsymbol{M}_{\text{total}} \propto \int \boldsymbol{M} \mathrm{d}V.$$

In thermal equilibrium, there are more nuclear spins aligned with the field (lower energy) than against (higher energy). The population ratio for the two orientations is given by the ratio of Boltzmann factors, and in equilibrium there is no preference for

either direction perpendicular to the field. These two facts imply that in equilibrium $\boldsymbol{M} = \boldsymbol{M}_0\hat{\boldsymbol{z}}$.

The phenomenological Bloch equations (1946) describe relaxation phenomena:

$$\frac{\partial \boldsymbol{M}(\boldsymbol{r},t)}{\partial t} = \boldsymbol{M}(\boldsymbol{r},t) \times \gamma_g \boldsymbol{H}(\boldsymbol{r},t) - \frac{(\boldsymbol{M}_z(\boldsymbol{r},t) - (\boldsymbol{M}_0(\boldsymbol{r},t))\hat{\boldsymbol{z}}}{T_1} - \frac{\boldsymbol{M}_x(\boldsymbol{r},t)\hat{\boldsymbol{x}} + \boldsymbol{M}_y(\boldsymbol{r},t)\hat{\boldsymbol{y}}}{T_2}. \quad (3.3)$$

Here, T_1 and T_2 are the spin-lattice and spin-spin relaxation constants, respectively. At equilibrium,

$$\frac{\partial \boldsymbol{M}(\boldsymbol{r},t)}{\partial t} = 0, \quad (3.4)$$

and $\boldsymbol{M}\boldsymbol{r}, t = \boldsymbol{M}_0\hat{\boldsymbol{z}}$ as required above. In the absence of relaxation, the Bloch equations, (3.1) apply (i.e. $T_1 = T_2 \to \infty$). Physically, $1/T_1$ is the rate at which the spins relax back to equilibrium, and $1/T_2$ is the rate at which spins lose coherence in the plane transverse to the static field (i.e. the x, y plane). T_1 is necessarily greater than or equal to T_2.

In a time short compared to T_2, the magnetization vector may be rotated to any angle, α, using an α-pulse. In particular, if a $\pi/2$-pulse is applied in the x-direction to an equilibrium spin system, then $\boldsymbol{M} = \boldsymbol{M}_0\hat{\boldsymbol{y}}$ in the rotating frame, or in the lab frame $\boldsymbol{M} = \boldsymbol{M}_0(\cos(\omega_L t)\hat{\boldsymbol{x}} + \sin(\omega_L t)\hat{\boldsymbol{y}})$. MRI experiments measure the signal from this rotating vector with an r.f. antenna or coil which can both receive and transmit transverse signals. In the discussion below, we will write the transverse magnetization, $\boldsymbol{M}_T$, in complex notation: $\boldsymbol{M}_T = \boldsymbol{M} = \boldsymbol{M}_x + \mathrm{i}\boldsymbol{M}_y$, where $\mathrm{i} = \sqrt{-1}$.

Next we examine the signal received from a small volume element (voxel) at position, $\boldsymbol{r}$, and time, t, after a $\frac{1}{2}\pi$-pulse. We assume that this process occurs for a time short compared to T_2 and that the magnetic field consists of a uniform part plus a gradient term:

$$\boldsymbol{H}(\boldsymbol{r},t) = (\boldsymbol{H}_0 + \boldsymbol{G}t \cdot \boldsymbol{r})\hat{\boldsymbol{z}} + \cdots. \quad (3.5)$$

The signal is proportional to

$$\boldsymbol{M}(\boldsymbol{r},t) = \mathscr{M}(\boldsymbol{r}_0,t_0)\exp(\mathrm{i}\Phi(\boldsymbol{r},t)), \quad (3.6)$$

where

$$\mathscr{M}(\boldsymbol{r}_0,t_0) = |\boldsymbol{M}(\boldsymbol{r},t)|$$

cannot change in time since we are neglecting T_2. Also,

$$\Phi(\boldsymbol{r},t) = \arg(\boldsymbol{M}(\boldsymbol{r},t)),$$

and $\boldsymbol{r}_0$ is the position of the voxel at the end of an excitation, which occurred at time t_0. From (3.2),

$$\Phi(\boldsymbol{r},t) = \int_{t_0}^{t} \omega(\boldsymbol{r},s)\,\mathrm{d}s = \gamma_g \int_{t_0}^{t} (\boldsymbol{H}_0 + \boldsymbol{G}(s)\cdot\boldsymbol{r})\,\mathrm{d}s. \quad (3.7)$$

Combining (3.6) and (3.7) with the assumption, for the moment, that the voxels do not move, and integrating over all space, we obtain the total signal, S, from all voxels:

$$S(t) = A_0 \exp(-\mathrm{i}\Phi_0)\exp(\mathrm{i}\boldsymbol{k}t) \int_{\textit{all space}} \boldsymbol{M}(\boldsymbol{r}_0,t_0)\exp(\mathrm{i}\boldsymbol{k}(t)\cdot\boldsymbol{r}_0)\,\mathrm{d}^3\boldsymbol{r}_0. \quad (3.8)$$

Here, A_0 is a proportionality constant, $\Phi_0 = \omega_L t_0$, and

$$\boldsymbol{k}(t) = \gamma_g \int_{t_0}^{t} \boldsymbol{G}(s)\,\mathrm{d}s. \quad (3.9)$$

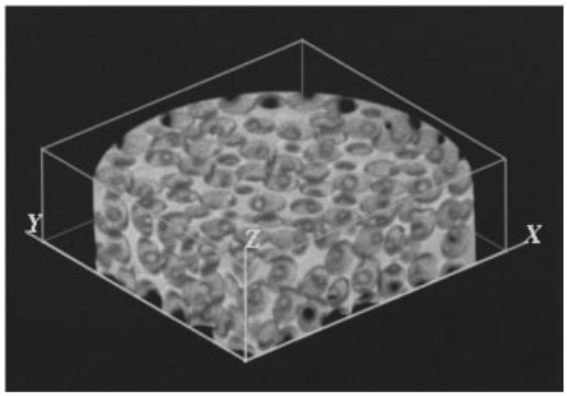

FIGURE 2. MRI volumetric rendering of the interstitial space (filled with water) in a packed bed. The section consists of 3.204 ± 0.029 mm diameter mono-disperse spherical acrylic beads poured into a 3.175 cm inner diameter tube. The intensity of the grey scale corresponds to the density of water at that point. This is a small section from a $256 \times 256 \times 256$ isotropic array. The spatial resolution is 0.140 mm.

The time dependence, $\exp(\mathrm{i}\omega_L t)$, can be removed by demodulation leaving the signal in (3.8) a function of $\boldsymbol{k}(t)$. In this context, $S(\boldsymbol{k})$ is the Fourier transform of $\mathscr{M}(\boldsymbol{r}_0, t_0)$. By carefully selecting $\boldsymbol{G}(t)$, the function, $S(\boldsymbol{k})$ can be measured for all $\boldsymbol{k}$ on a grid. A fast Fourier transform yields $\mathscr{M}(\boldsymbol{r}_0, t_0)$, which is proportional to the density of spins, $\rho(\boldsymbol{r}_0, t_0)$.

Spatial encoding is the process of measuring the density of spins throughout space using magnetic field gradients. The largest value of the corresponding component of $\boldsymbol{k}$ on the grid determines the spatial resolution in a particular direction. With the gradients we have available, we can achieve resolutions of 5 μm. Typically, however, we use a resolution of 0.40 mm in order acquire images in a time which is short compared to τ_h. Since our media have a scale of 3 mm, this resolution is sufficient to obtain information on a scale comparable to the interstitial spacing of the beads.

In the next three figures, we present information on the distribution of pores in packings of plastic spheres. In figure 2, we show a three-dimensional reconstruction of a section of a porous medium consisting of spherical beads, of diameter 3.204 ± 0.029 mm which were also used in the convection experiments. These beads were placed without regard to spatial order in a plastic tube of diameter 3.175 cm between two perforated plugs 10 cm apart, and the resulting pore space was saturated with water. The image shows the relative density of the water with a spatial resolution of 0.140 mm using volumetric rendering. The beads do not produce an NMR signal.

The individual spheres in figure 2 exhibit a great deal of packing order near the wall of the cylinder, as expected. We further demonstrate this effect in figure 3, which shows the results of an azimuthal and lengthwise integration of the density of water in the cylinder. The resulting radial density of water shows spatial oscillations at a period corresponding to dense triangular packing of the spheres, i.e. the packing is not truly random but contains ordered domains. More insight into the ordering comes from figure 4 which shows in greyscale the radial density corresponding to a projection of the fluid-occupied volume onto a plane. Ordering occurs not only near the walls from the effect of gravitational packing, but, in an

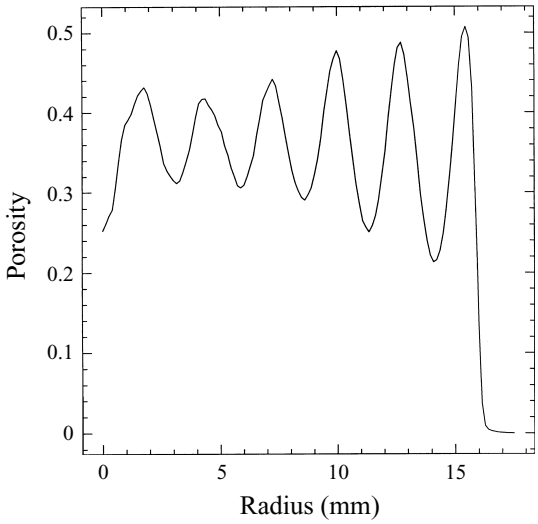

FIGURE 3. Porosity averaged azimuthally and over the $\hat{z}$-direction as a function of radius. A thick slice, which is 35 mm or 11 bead diameters thick was taken from a $256 \times 256 \times 256$ isotropic density acquisition shown in figure 2. The tube diameter is 3.175 mm.

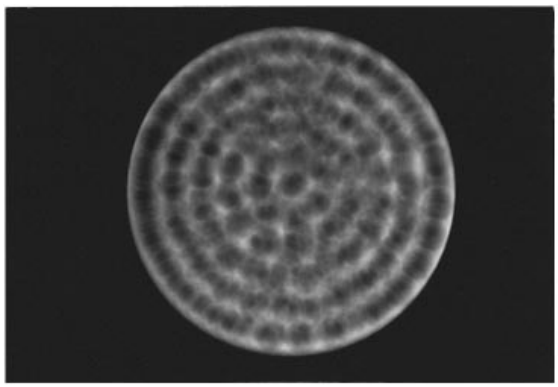

FIGURE 4. Projection of the fluid density from the previous image onto a plane, encoded in grey scale. The ordering of the spheres near the sidewall, and the propagation of the order into the interior of the cylinder is apparent.

average sense, everywhere throughout the cylinder. This effect is virtually impossible to avoid for mono-disperse spheres. We will return to this issue below when we consider results for PMC in media which consist of nominally random sphere packings.

Velocity encoding for a moving fluid is similar to spatial encoding, except that now the Lagrangian position of a spin, $\boldsymbol{r}$, is a function of t. Expanding $\boldsymbol{r}(t)$ in a Taylor series we obtain

$$\boldsymbol{r}(t) = r_0 + v_0 t + \cdots, \tag{3.10}$$

where v_0 is the velocity at the end of excitation. Combining (3.10) with (3.5) to (3.7), and integrating over all space and all velocities, neglecting acceleration and higher

terms from (3.10), we obtain the signal from all spins,

$$\mathrm{S}(\boldsymbol{k},\boldsymbol{q}) = A_0 \exp(-\mathrm{i}\Phi_0) \exp(\mathrm{i}\omega_L t) \iint\limits_{\substack{\text{all space}\\ \text{all velocities}}} \mathrm{M}(\boldsymbol{r}_0, v_0, t_0) \exp(\mathrm{i}(i(\boldsymbol{k}(t)\cdot\boldsymbol{r}_0 + \boldsymbol{q}(t)\cdot\boldsymbol{v}_0))\, \mathrm{d}^3\boldsymbol{r}_0\, \mathrm{d}^3\boldsymbol{v}_0. \tag{3.11}$$

Here

$$\boldsymbol{q}(t) = \gamma_g \int_{t_0}^{t} \boldsymbol{G}(s) s \, \mathrm{d}s. \tag{3.12}$$

Since $\boldsymbol{k}$ and $\boldsymbol{q}$ can be varied independently, equation (3.11) is sufficient to obtain $\mathscr{M}(\boldsymbol{r}_0, \boldsymbol{v}_0, t_0)$, which is proportional to the density, $\rho(\boldsymbol{r}_0, \boldsymbol{v}_0, t_0)$.

Because $\rho(\boldsymbol{r}_0, \boldsymbol{v}_0, t_0)$ is a six-dimensional function, and it takes time and computer memory to obtain and store each point, it is not practical at this time to measure this whole function. We employ two techniques to limit the sample to a manageable size. The first technique involves *selective excitation*, in which experimentally applied field gradients, in conjunction with r.f. pulses limit the spatial extent of the excitation to a slice of a thickness that is controlled by the strength of the gradient. That is, if the gradient is high, then only a thin slice will be at the correct frequency for the r.f. excitation. The second technique consists of averaging over one of the dimensions. This works well for the velocity as long as $\rho(v_x, v_y)$ does not vary significantly over a volume element $\mathrm{d}x\mathrm{d}y\mathrm{d}z$ (voxel). Using these procedures and a slice thickness Δz we typically measure the three-dimensional distribution

$$\rho(x, y, v_z) = \iint \int_{z-\Delta z/2}^{z+\Delta z/2} \rho(x, y, z, v_x, v_y, v_z)\, \mathrm{d}z \mathrm{d}v_x\, \mathrm{d}v_y. \tag{3.13}$$

We obtain the distribution of velocities, and the porosity from $\rho(x, y, v_z)$. The average value of $v_z(x, y)$ is then $\int \rho(x, y, v_z) v_z \, \mathrm{d}v_z$. As with spatial encoding, the finest velocity resolution of 0.02 $\mathrm{mm\,s^{-1}}$is in practice set by the strength of the gradients.

We also can measure the local temperature with MRI, since T_1 is a function of temperature. In the above analysis we have ignored this temperature-dependent relaxation for convenience. A full analysis reveals the temperature dependence, and allows the possibility of exploiting this dependence to obtain local temperatures.

Although the primary goal of the present experiments is to characterize the flows in PMC, we have carried out two other simpler experiments in order to test MRI velocity encoding. The first of these was simple Poiseuille flow of water through a cylinder, i.e. without any porous media present. The second was the porous analogue of Poiseuille flow through a cylinder, except now the cylinder was filled with a porous medium consisting of plastic spheres.

In the first experiment, we measured the velocity in a long open pipe of circular cross-section. We compare the results with the theoretical profile in figure 5. Because we measured the volumetric flow rate to an accuracy of $\pm 1\%$, there are no fitted parameters in the comparison of theory to measurement. The agreement between theory and experiment is excellent.

In figure 6 we show the parallel results for flow through a porous-medium-filled cylinder (Georgiadis *et al.* 1991). These images are obtained by averaging over the 2 mm slice thickness according to (3.13), where in this case, the z-direction corresponds to the axial direction. An interesting feature of these experiments is that the overall distribution of velocities is exponential, a result which has been obtained theoretically by Martys, Torquato & Benz (1994).

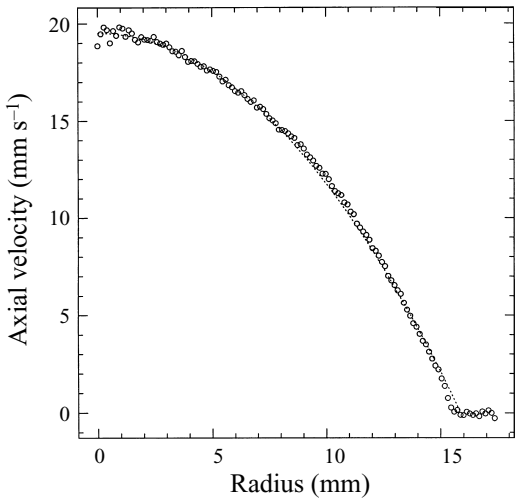

FIGURE 5. Comparison of the azimuthally averaged velocity along a 3.175 cm pipe to the theoretical parabolic prediction. The velocity is averaged over a 2 mm thick slice and over the azimuthal angle. The spatial resolution is 140 μm, and the velocity resolution is 0.6 mm s^{-1}. The theoretical velocity profile, shown as a dotted line, is based on the measured flow rate and the geometry of the tube. There are no fitted parameters.

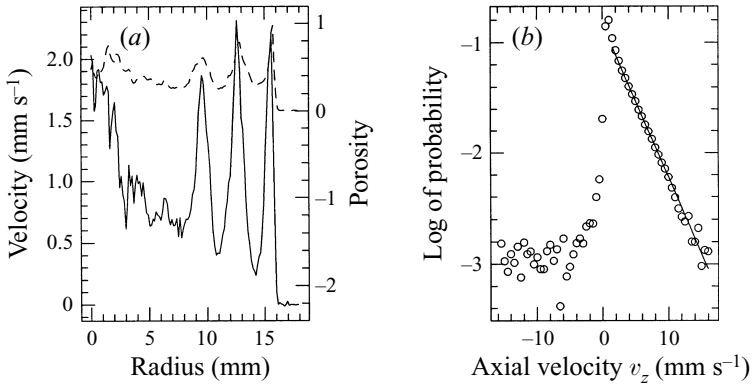

FIGURE 6. (*a*) Azimuthally averaged fluid density (dashed line) and velocity (solid line) within a 2 mm slice for flow in a pipe filled with beads. (*b*) The distribution of longitudinal velocities in this experiment, without regard to position, is an exponential function of v_z.

3.2. *Experimental convection apparatus*

The primary thrust of these experiments concerns PMC. To this end, we have constructed a convection cell, sketched in figure 7, which closely approximates the theoretical ideals of uniform temperatures and rigid boundaries at the top and bottom. The cell consists of horizontal parallel isothermal planes, constructed from 1 mm thick aluminium nitride (AlN) plates, separated a distance H by a machined Delrin spacer. The sealed water-saturated sample of porous medium, confined by the AlN plates and spacer, resides in an outer Delrin container with a large number of flow ports. These ports provide cooling water to the top and heating water to the bottom of the convection layer.

In a conventional RBC cell, at least one of the horizontal bounding plates would be copper. But, because of the r.f. and rapidly changing magnetic fields produced

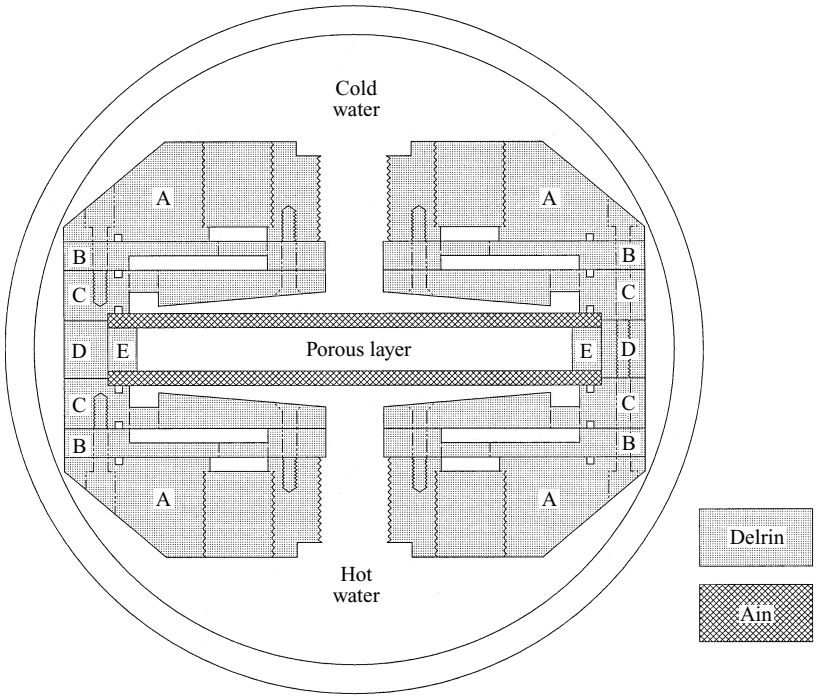

FIGURE 7. Schematic of convection cell. Hot water flows in the bottom section and cold water flows in the top section. The outer circle represents the bore of the magnet, which is 15.24 cm in diameter. Letters A–D indicate different parts of water distributors and outer casing. E is the spacer.

during MRI, no metal could be used in the construction of the convection cell. In place of copper, we used AlN, a ceramic, with both high electrical resistivity and high thermal conductivity, 1.33 $\mathrm{W\,cm^{-1}\,K^{-1}}$. AlN has 1/3 the thermal conductivity of copper, 222 times the thermal conductivity of water, and 3.3 times the thermal conductivity of sapphire, which is often used in high-precision convection experiments with shadowgraph visualization. The high conductivity ensured that the plates were isothermal and that horizontal temperature gradients were minimized.

The two AlN plates were held at constant temperatures by two separate temperature-controlled water reservoirs that provided circulating water to the ports in the outer Delrin container. The baths were controlled by a laboratory computer using proportional and integral feedback to a stability of 5 mK. Thermistors at the inlets and outlets to the Delrin outer container determined the temperatures of the AlN plates to 0.3 mK. These thermistors were measured using a scanning digital multimeter connected by an IEEE interface to the laboratory computer. There was no detectable difference in the inlet and outlet temperatures of either of the two circulating bath streams. This indicates that the temperatures measured outside the cell were good representations of the actual temperatures of the top and bottom plates.

During the course of the experiments, we used three different Delrin spacers, each with a different planform (see table 1). In each case, the thickness, H, varied by less than 25 μm around the spacer. The careful machining, along with the use of a levelling bubble ensured that the top and bottom plates were horizontal and parallel. To construct the solid matrix of the porous medium, we used 3.204 ± 0.029 mm mono-disperse acrylic spheres. We used distilled, deionized water to fill the cell.

Planform	Height (mm)	Width (mm)	Length (mm)	Γ
Circular	9.52	radius = 47.60	na	5.00
Rectangular	10.95	51.70	87.20	7.97
Hexagonal	10.69	96.80 (corner to corner)	na	9.05

TABLE 1. Physical dimensions of various spacers.

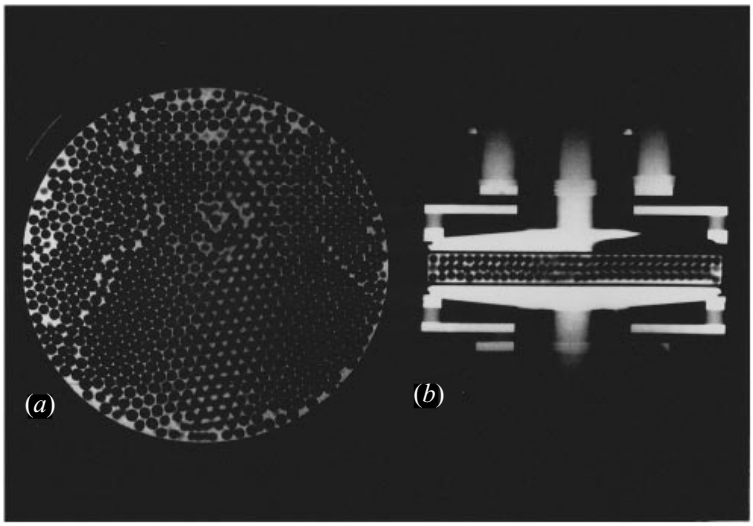

FIGURE 8. (*a*) Density MRI of a 1 mm horizontal slice of the disorder medium. The slice is taken at approximately mid-plane. (*b*) Density MRI of a 8 mm vertical slice of the disordered medium and Delrin cell. The cooling/heating water also appears in this image.

To obtain a nominally disordered packing, we poured the spheres into the circular cell and sealed it. Figure 8(*a*), a density image, reveals that the disordered packing is far from random and contains several ordered regions meeting at grain boundaries as well as other defects. Figure 8(*b*) shows that the cell is packed 3 bead-layers high. To obtain the ordered packing in the rectangular and hexagonal cells, we carefully packed the beads into a 4-layer triangular ABCA lattice (Ashcroft & Mermin 1976).

We also measured the heat transport across the convective layer. In more conventional experiments, this is typically an easy measurement to make through the use of resistive heating. However, we found that the presence of the heater, a conductor, interfered with the r.f. field needed for MRI, and we were obliged to use a different technique. We added two extra layers to the bottom AlN plate. With the extra layers in place, the bottom plate consisted of a thin sheet of lexan sandwiched between two highly conducting AlN plates, as in figure 9. Since there were only vertical boundaries between the isothermal plates, the heat flux q was constant in each region. The total heat current through the sandwich was $Q_s = A_s q_s$, where A_s was the area of the sandwich perpendicular to the direction of heat flow. Likewise, the total heat current through the Delrin spacer was $Q_D = A_D q_D$, where A_D was the area of the spacer, and the total heat current through the medium was $Q_m = A_m q_m$, where A_m was the area

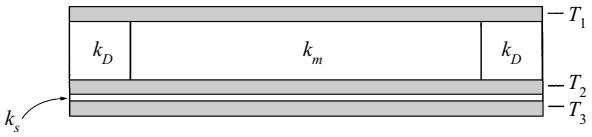

FIGURE 9. Cross-section of experimental cell for MRI and *Nu* measurements, showing the Delrin spacer, and *Nu* measurement sandwich. T_1, T_2, and T_3 are measured temperatures. k_D, k_s, and k_m are the conductivity of the Delrin spacer, the sandwich, and the medium, respectively.

of the medium. By conservation of energy, $Q_s = Q_D + Q_m$. Solving for k_m, we obtain

$$k_m = \frac{C_s(T_1 - T_2)/(T_1 - T_3) - A_D k_D}{A_m}. \tag{3.14}$$

Here, $C_s = A_s k_s H/h$ and h is the height of the sandwich. The temperatures T_i are defined in figure 9. We determined C_s using the following rearrangement of (3.14) and the known conductivity of the medium below onset using (table 2):

$$C_s = (A_m k_m + A_D k_D)\left(\frac{T_1 - T_3}{T_1 - T_2}\right)_0. \tag{3.15}$$

The 0 subscript refers to measurements below onset. Combining (3.14), (3.15), and (2.38) we obtain

$$Nu = (1 + \Lambda)\left(\frac{T_1 - T_2}{T_1 - T_3}\right)\left(\frac{T_1 - T_3}{T_1 - T_2}\right)_0 - \Lambda, \tag{3.16}$$

where $\Lambda = (A_D k_D)/(A_m k_m)$. For the hexagonal cell, the relation $k_m = \phi k_w + (1 - \phi)k_p$ leads to the simple result: $\Lambda = 1.0$. Here, k_w is the thermal conductivity of water, k_p is the conductivity of the plastic beads, and ϕ is the porosity of the medium. In general, the conductivity of the medium must be known to use (3.16) to calculate *Nu*.

For the experiments using disordered media, the *Nu* measurement sandwich was not in place, and our determination of ΔT_c was no better than 20%. For experiments with the rectangular cell, we determined ΔT_c from images at 0.5 K increments, which gave a relative accuracy of $\pm 2.5\%$ in ΔT_c. For the experiments with the hexagonal cell, we used both images and *Nu* to determine ΔT_c.

The determination of *Ra*, and Ra_c in particular, with absolute accuracy is complicated by the fact that the permeability is difficult to measure. By contrast, the remaining parameters contained in *Ra* are fairly well known, particularly, ΔT_c. However, ϵ only depends on ΔT and ΔT_c, to the extent that all other parameters in *Ra* are constant. We will use ϵ exclusively, where it is understood that $\epsilon = (\Delta T - \Delta T_c)/\Delta T_c$.

Information on γ is also useful. We made two estimates of this quantity. First we used (2.2). We can estimate the permeability from (2.2), but the accuracy of the estimate is unlikely to be very high. Second, we calculated γ from the definition of $Ra_c = 4\pi^2$, the measured ΔT_c and the medium and the material properties. Table 2 presents the results of these two estimates, which differ by a factor of 2.75.

4. Results

4.1. *Introduction*

In this section, we present results for three different planforms: circular, rectangular, and hexagonal. This sequence follows a natural order from least to most packing

Parameter	Water at 40 °C	Beads (plastic)	Medium
Thermal expansion α (K^{-1})	3.8530×10^{-4}	6.8×10^{-5}	na
Thermal conductivity k ($W\,cm^{-1}\,K^{-1}$)	6.27×10^{-3}	1.9×10^{-3}	3.0×10^{-3}
Density ρ ($g\,cm^{-3}$)	0.9922158	1.19	1.14
Specific heat c ($J\,g^{-1}\,K^{-1}$)	4.1786	1.470	2.173
Kinematic viscosity v ($cm^2\,s^{-1}$)	6.580×10^{-3}	na	na
Permeability γ (cm^2):			
random, $\phi = 0.31$	na	na	4×10^{-5}
close-pack, $\phi = 0.26$	na	na	2×10^{-5}
close-pack, based on ΔT_c	na	na	5.5×10^{-5}

TABLE 2. Material parameters. (Unless otherwise noted, medium properties are for the close-packed cell and are calculated based on an average of the separate properties weighted by the porosity.)

order of the spheres in the convection layer. These results consist of data for the vertical velocity as a function of the horizontal coordinates, as well as *Nu* data.

Before turning to the details of these results, we consider the effects of averaging the velocity in the vertical direction. Typically, we obtain results for the vertical velocity by exciting the spins in a horizontal slice of the cell. We obtain the best signal quality by choosing this slice to be essentially the entire height of the convection layer. To justify this process, we obtained images for 2 mm and 8 mm slices of the convection cell. The 2 mm slice did not convey any more information than the 8 mm, and the 8 mm slice had better signal-to-noise ratio due to the spatial averaging. In this work we will display only images with 8 mm slice thickness. In all the images, we make a small uniform correction of the velocities, such that the net flow rate is zero. This correction is about 2% of full scale.

4.2. *Disordered media*

Pattern selection in the disordered medium (aspect ratio $\Gamma = radius/H = 5.00$) is dominated by defects in the packing. In figure 10, we show velocity images for the disordered medium at several values of ϵ. This is the same medium as in figure 8. In this figure and the following figures, we use greyscale to encode the vertical velocity. Darker regions correspond to upflows, and lighter regions to downflows.

Figure 10(*a*) shows the circular cell for $\Delta T = 0$. In figure 10(*b*), $\epsilon = -0.5$, and convection has begun near the wall and at the grain boundaries. The latter are evident in figure 8(*a*). Convection occurs first in these places because the porosity, and hence the permeability, γ are locally largest in these regions. As ϵ increases above onset to 1 (figure 10*c*), convection occurs in the regions of ordered sphere packing. We define ΔT_c to correspond to the onset of convection within the interior of the cell and away from defects. The convection along the grain boundaries is stronger than in the bulk and tends to pin the pattern even with increasing ϵ, as seen as in figure 10(*d,e*). In this sequence, the pattern changes little, especially near the defects. By contrast, the patterns obtained for ordered packings change considerably for the same range of ϵ, as in figures 12 and 13. To emphasize the pinning effect of the defects, figure 10(*f*) shows the pattern after we dropped ΔT to 0 and returned it to $\epsilon = 3$. The pattern in (*f*) is very similar to that in (*d*) and (*e*), i.e. the defects tend to produce the same pattern on cycling through onset. By contrast, the ordered media, figure 13, show different patterns when they are cycled through onset.

Estimates of the wavenumber for the patterns in this cell range from $q = 0.8\pi$ to $q = 3\pi$. The lower end of this range corresponds to the interior of the cell where

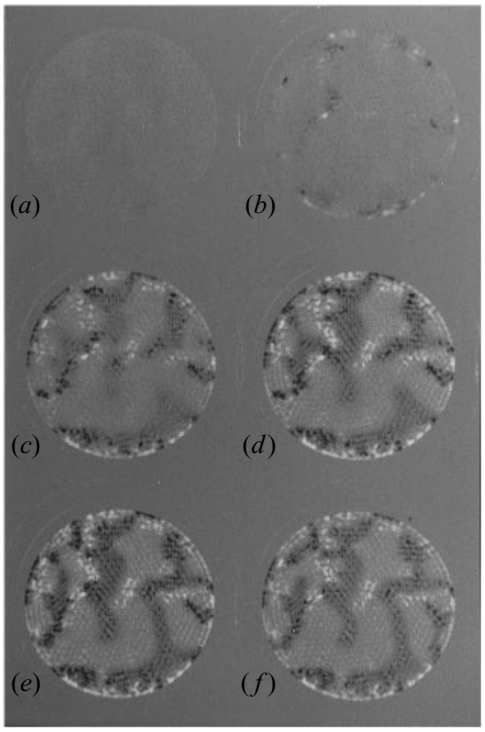

FIGURE 10. Vertically averaged, vertical velocity for a circular cell with disordered packing. (*a*) $\Delta T = 0.0$, $\epsilon = -1.0$. (*b*) $\epsilon = -0.5$. (*c*) $\epsilon = 1.0$. (*d*) $\epsilon = 3.0$. (*e*) $\epsilon = 5.0$. (*f*) $\epsilon = 3.0$, but after first decreasing ΔT to 0, and then raising it back to $\epsilon = 3$.

there are no defects. The upper end of this range corresponds to the very short rolls which form near the defects and walls. Due the modest aspect ratio and the presence of defects, the wavenumber in the cell interior is not sharply defined, although it is definitely smaller than π. For instance, $q = \pi$ would correspond to 5 roll pairs across the diameter, whereas we observe 4 to 4.5 pairs. A surprising observation is that the regions of upflow are smaller, on average, than the regions of downflow; we observe a comparable effect in the ordered media. Although not as pronounced as in the ordered media, the ratio of the size of up-flowing regions to down-flowing regions decreases as ϵ increases.

The striking effect of the packing defects on the pattern formation is exacerbated by the small number of layers. One missing bead from an area of close packing can change ϕ by a third. For the reasons discussed in §2.3, we cannot increase the number of layers by an amount which would significantly decrease the impact of a defect.

4.3. *Ordered media*

Because the defects in the disordered medium strongly perturb the system, ordered media are much more likely to approach the ideal case of a homogeneous medium envisaged in most theoretical models. Nevertheless, experimental systems with regular sphere packing must, in general, still have periodic spatial variations which are at most an order of magnitude smaller than a convective wavelength, and depending on the packing scheme, there may also be large effective variations in the permeability at the sidewalls.

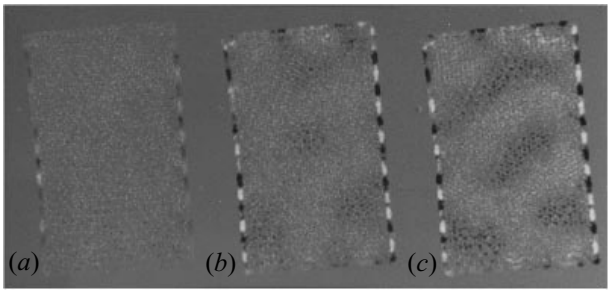

FIGURE 11. Vertically averaged, vertical velocity for a rectangular cell with ordered packing for various values of ϵ: (*a*) -0.5, (*b*) 0.2, (*c*) 0.4.

In the ordered media, we used packings with hexagonal symmetry. We began our investigation with a rectangular planform with an aspect ratio in the long direction of $\Gamma = 7.97$ (table 1). Consequently, the packing along the short and the long sidewalls of the container differ. In our packing $\phi_L > \phi_S > \phi_{bulk}$, where ϕ_L, ϕ_S, and ϕ_{bulk} are the porosities near the long wall, the short wall, and the interior, respectively. Equations (2.2) and (2.16) suggest that the flows will be qualitatively different near the long and short walls, as well as in the interior of the layer. This expectation is consistent with our observations.

Figure 11 shows the progression of the patterns for the rectangular cell as ϵ increases. Convection begins first along the long wall (figure 11*a*) at $\epsilon = -0.5$. The wavenumber, q_L, in this region is 2.05π, which is typical for the defect regions and is larger than the value π predicted for the bulk porous medium. Convection begins on the short wall at $\epsilon = -0.2$ and in the bulk, or interior, at $\epsilon = 0$, by definition. The wavenumbers in these regions are $q_S = 1.35\pi$ and $q_{bulk} = 0.77\pi$, for the short wall and the bulk, respectively, as seen in figure 11(*b*, *c*). The wavenumber for the interior, q_{bulk}, which is the only wavenumber which we can reliably compare to theory, is measurably smaller than predicted. It is interesting that $q_L > q_S > q_{bulk}$.

The fact that well-defined convection rolls without pinning form in the rectangular planform experiment indicates that, within the context of PMC, uniform packings are more like the homogeneous media envisaged in models, than disordered packings. However, a more desirable situation would be one in which the sidewalls were identical. One possibility would be square packings of spheres. However, such packings are gravitationally unstable, and tend to collapse into close-packing arrangements. To achieve uniformity at the walls, with hexagonal sphere packings it is necessary to have a planform with hexagonal symmetry. The following experiments were carried out in such a geometry.

Using the $\Gamma = 9.05$ convection cell with hexagonal planform, we studied states from $\epsilon < 0$ to $\epsilon = 7$. We document representative states in figures 12 and 13. With increasing ϵ, we see the following sequence. For $\epsilon < -0.4$, we do not observe any flow, within our resolution, and the Nusselt curve is flat. At roughly $\epsilon = -0.4$, we first discern localized convection rolls near the sidewalls with $q \simeq 1.1\pi$. These localized rolls do not contribute measurably to the Nusselt number which remains flat within our resolution to $\epsilon = 0.0$. We first detect convection in the bulk (i.e. in the interior) with MRI for $\epsilon \simeq 0.15$. There is a sharp increase in Nu above ΔT_c, and this sharp bifurcation allows us to determine ΔT_c to within 1% by fitting Nu above and below onset, and by then determining the intersection of these two parts of the heat transport curve.

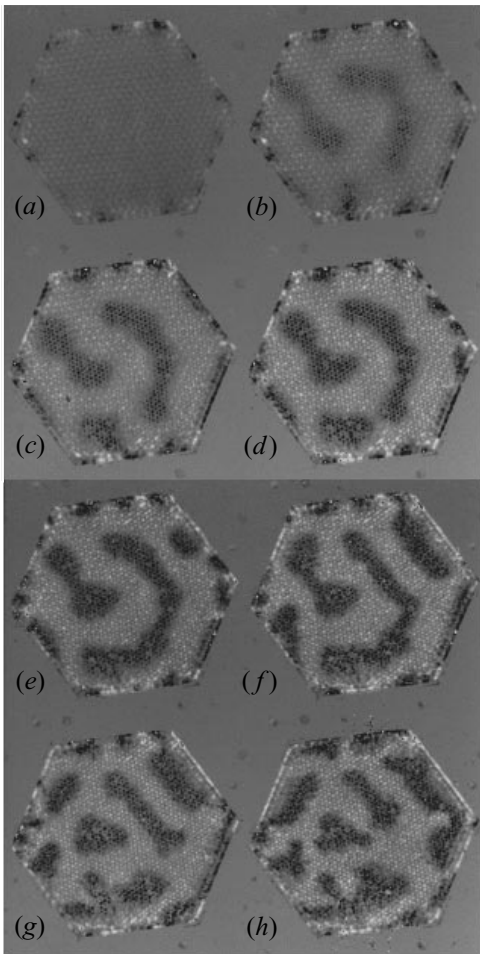

FIGURE 12. Vertically averaged, vertical velocity for hexagonal cell with ordered packing. (*a*) $\epsilon = -0.2$. (*b*) $\epsilon = 1.0$. (*c*) $\epsilon = 2.0$. (*d*) $\epsilon = 3.0$. (*e*) $\epsilon = 4.0$. (*f*) $\epsilon = 5.0$. (*g*) $\epsilon = 6.0$. (*h*) $\epsilon = 7.0$.

We observe steady convection for $0.15 \leqslant \epsilon < 5.0$. At the upper end of this range, the pattern, though steady, no longer consists of rolls, but rather is a cellular pattern. This pattern is a precursor of the time-dependent states for $\epsilon \geqslant 6$; in these states the smaller upflow regions move, apparently randomly, in a larger sea of downflow.

In the steady regime, the sidewalls appear to play only a minor roll in pattern formation. For instance, figure 13 shows four different patterns formed at $\epsilon = 1$, after repeated cycling of ΔT below ΔT_c. Substantially different patterns form in the bulk on each cycling. Unlike the case of RBC, the nominally slip boundary conditions in PMC do not force the rolls to be perpendicular at the boundaries. In these images, rolls are both perpendicular and parallel to the walls. Some patterns have more symmetry than others, and the rolls may also branch as in figure 13(*c*).

As discussed in §2.4, we expect that the vertical vorticity should decay rapidly to zero within the stability region. Hence, the complex, often time-dependent states of low to moderate Pr in RBC which result from coupling of vertical vorticity to mean flows, should be absent in PMC. To test this, we brought the system to $\epsilon = 7$, which is a relatively rapidly changing time-dependent state. From this state, the system

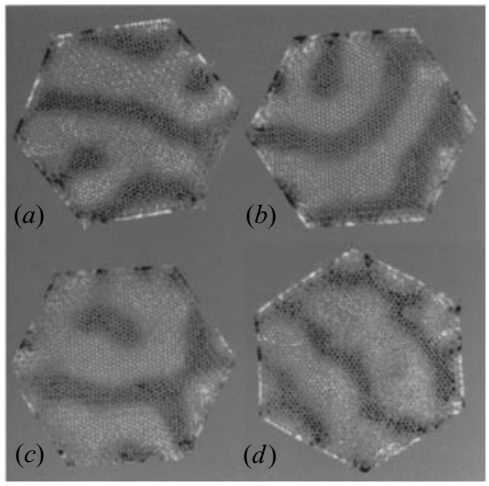

FIGURE 13. Vertically averaged, vertical velocity for hexagonal cell with ordered packing at $\epsilon = 1$, but ΔT was dropped to 0 between each image.

was quickly quenched to ϵ within the stability region, $\epsilon \leqslant 5.0$. Figure 14 shows a representative sample of this process. Each image except for the last is separated by $2\tau_v$. In figure 14(a, b), the system is in the time dependent state at $\epsilon = 7$. Between figure 14(b) and figure 14(c), we reduced ϵ, in $0.3\tau_v$, to $\epsilon = 2$. Figure 14(c–e) shows the decay to a steady state, and figure 14(f) shows the pattern $100\tau_v = 1.2\tau_h$ after figure 14(c). We carried out similar quenches from $\epsilon = 7$ to $\epsilon = 0.2$, 1, 3, and 4. In each case, the system approached a steady state in $2\tau_v$–$5\tau_v$ and was stable for up to τ_h, except for minor adjustments in the wall regions. Presumably, the pattern would have remained stable beyond τ_h, although we cannot be sure of this expectation.

An interesting issue is the evolution of the wavenumber with varying ϵ. Figure 12 shows the patterns, from which we can determine q, over $\epsilon = 0$ to $\epsilon = 7$. At onset, $q_c = 0.7\pi$, which does not match the theoretical prediction of $q_c = \pi$. We tentatively attribute the difference between theory and experiment to competition between the structure of the medium and the conventional wavelength selection process. In light of this difference, we present in figure 15 data for ϵ versus reduced wavenumber, $Q = (q - q_c)/q_c$, for various runs. We also include in this figure the theoretical stability boundaries, Straus (1974), where we have chosen q_c for the data and the predictions so that the two curves agree at $Q = 0$.

Figures 12 and 13 indicate that there is an asymmetry between the horizontal size of the upflowing and downflowing rolls. Figure 16 shows this effect explicitly in terms of λ_u/λ_d, the ratio of the wavelength determined from the up- and downflowing regions for the various runs. This ratio steadily decreases with increasing ϵ. Correspondingly, the area occupied by upflowing rolls decreases with increasing ϵ. By $\epsilon = 5$, figure 12(f), the pattern has become cellular, with small regions of faster upflow moving in large regions of slower downflow. We tentatively ascribe this asymmetry to the relatively large temperature differences which occur at large ϵ. These large differences imply a breaking of the up-down symmetry. Similar temperature differences may occur in RBC experiments. But, in that case, other effects, such as vorticity coupled to mean flows, which leads to time dependence, may mask the effect which we observe here. Although a theory exists to describe departures from the Boussinesq approximation

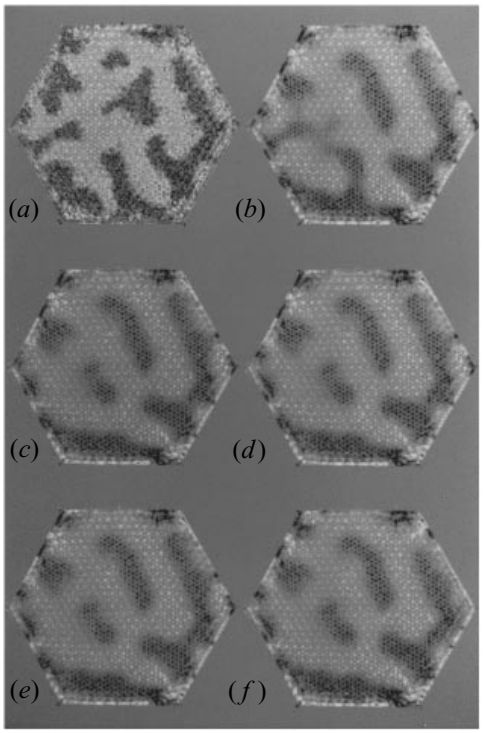

FIGURE 14. Vertically averaged vertical velocity for hexagonal cell with ordered packing. This sequence shows the effect of a temperature quench. All images, except for the last, are $2\tau_v$ apart. (*a–b*) $\epsilon = 7$. Time-dependent state before quenching ΔT. (*c–e*) Decay to steady state at $\epsilon = 2$. (*f*) State $100\tau_v$ after quench.

in RBC near onset, we know of no comparable theory which would address the current experiments.

As noted previously, the time-dependent states which occur for $\epsilon > 6.0$ are qualitatively different from the expected cross-roll state (Straus 1974). Figure 17 shows the time-dependent motion at $\epsilon = 7$ through a series of images which are separated in time by $2\tau_v$. The motion is not obviously periodic, although we do not have enough data at this time to definitively establish this point.

In two runs we included our *Nu* measurement device, and the results from these measurements are given in figure 18. We did not use this device routinely, because there are some differences in the pattern which formed while using it. For instance, in figure 13(*d*) we include an example of the pattern with the device in place, whereas for the other images in that figure, this device was not in place. With the *Nu* apparatus, the roll boundaries are not as smooth, there is more branching, and the upflow region is thinner at the same ϵ. Although there is clearly some perturbative effect with the *Nu* device in place, the important point is that, within our resolution, the bifurcation to convection is sharp, and measurements of *Nu* determine ΔT_c precisely. By determining ΔT_c precisely, we observe that the small rolls next to the walls have only a minimal effect on the heat transport. For instance, the left-hand arrow in figure 18 indicates where we first detect convection next to the wall using MRI, and the right-hand arrow indicates where we can first detect flow in the bulk. The critical temperatures for the two runs differ by 6%, which is within our experimental resolution, and presumably is related to differences in the pattern. Specifically, the values are $\Delta T_c = 8.5$ K and

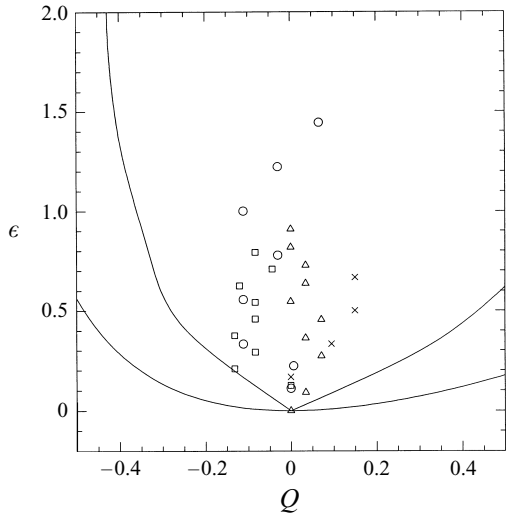

FIGURE 15. ϵ versus reduced wavenumber, $Q = (q-q_c)/q_c$, where q_c is the experimentally determined wavector, $q_c = 0.7\pi$. The curves indicate the predicted stability boundaries, shifted to line up with the experimental q_c.

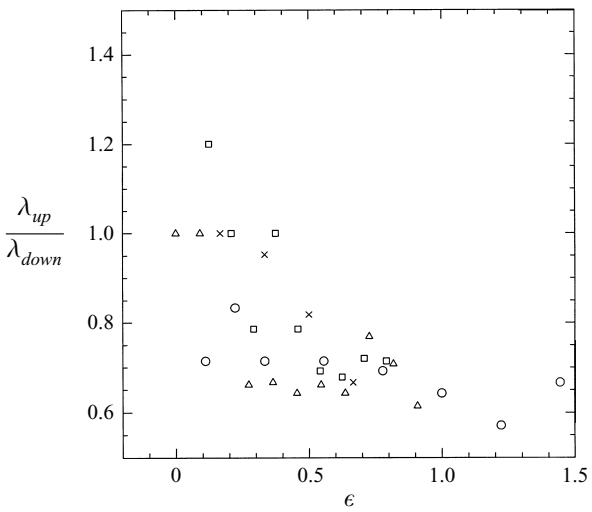

FIGURE 16. Ratio of upflowing roll width to downflowing roll width versus ϵ.

$\Delta T_c = 8.0$ K. The average slope

$$S = (\mathrm{d}Nu/\mathrm{d}\epsilon)_{\epsilon\to 0^+} \tag{4.1}$$

of both curves is 0.73 ± 0.05, which differs from the theoretical value of 2. By comparison, other experimenters have found comparable or smaller slopes. For instance, Elder (1967) found $S = 1$, and Howle *et al.* (1997) find a slope between 0.53 and 1.35, depending on the medium. Close *et al.* (1985) find that the slope is dependent on the the ratio d/H, where systems having larger values of this ratio had lower S.

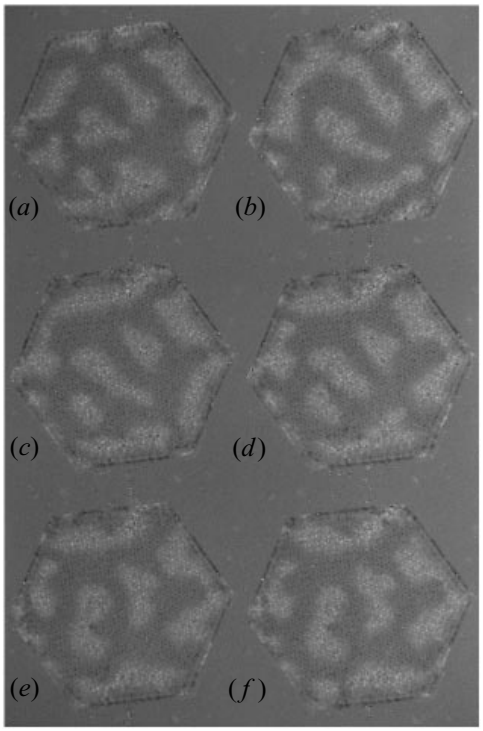

FIGURE 17. Vertically averaged, vertical velocity for hexagonal cell with ordered packing showing time-dependent behaviour above 6ϵ. The images are separated by $2\tau_v$ and are for $\epsilon = 7$.

5. Summary and conclusions

In the present study and the following parallel work by Howle *et al.*, we describe non-invasive experimental tests of theories for convection in porous media. These experiments provide information on pattern selection and high-precision heat transport data. In particular, the present experiments provide local information on the fluid velocity, both for convecting fluids and for pressure-driven flows. Several of the theoretical predictions are not well satisfied. We identify the modest size of the ratio d/H as the key reason for the differences between theory and experiment. Specifically, for typical experiments consisting of bead packings, the assumption of homogeneity, which requires $d/H \ll 1$ is not satisfied. Although there may be alternative ways to construct porous media which are effectively homogeneous, large classes of porous systems are subject to three conflicting constraints: the requirement that d/H is small, the requirements for Boussinesq conditions, and the need for tractable relaxation times. Given d/H only modestly small, the structure of the medium will play a role which is not considered in conventional theories. Consequently, the assumption of homogeneous Darcian flow, which has routinely been used in the past, needs improvement or replacement for the PMC problem.

The medium structure affects pattern formation in several ways. For nominally disordered arrangements of spheres, packing defects such as grain boundaries between locally ordered packing regions, lead to complex cellular convection patterns which are pinned by the defects. In ordered sphere packings, well-defined convection rolls, which differ in detail on repeated cyclings through convective onset, occur in the interior of the container, and small-wavelength rolls occur near the walls. However,

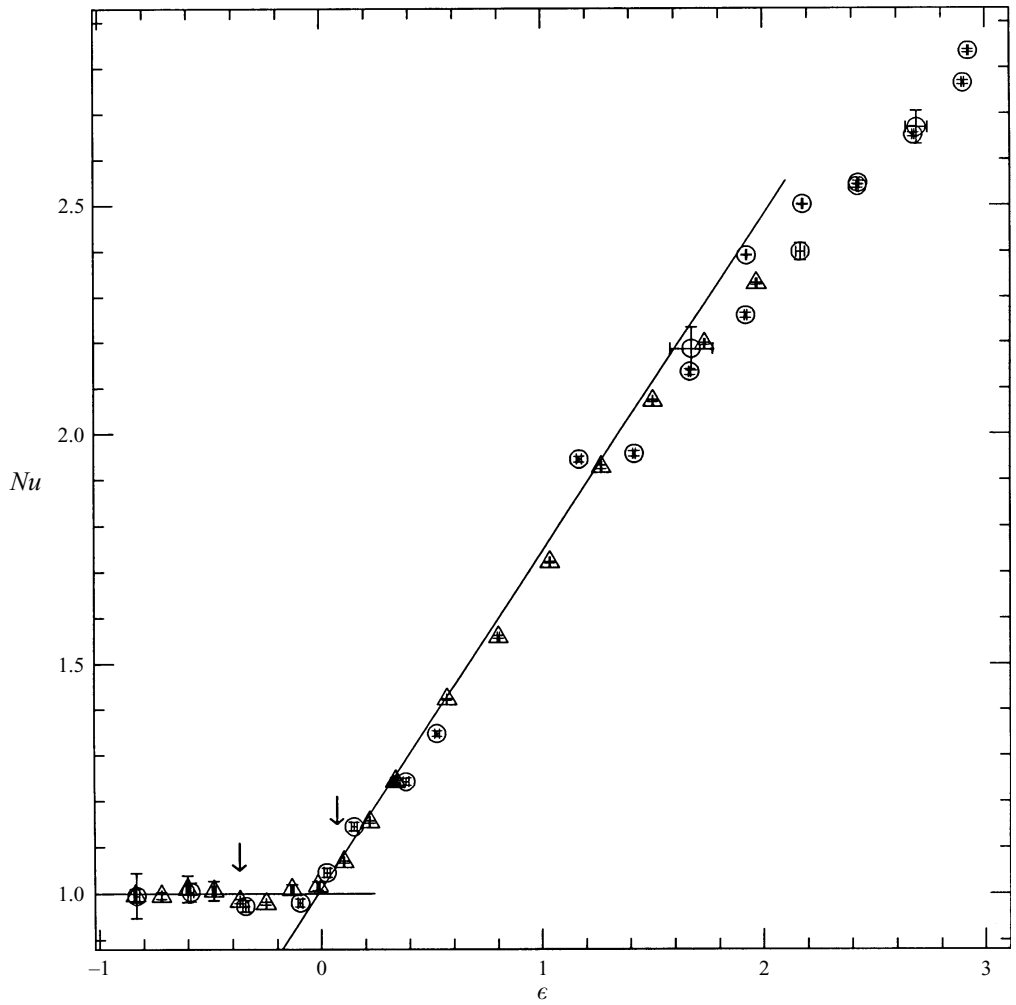

FIGURE 18. *Nu* versus ϵ, for two different runs with the hexagonal cell.

the wavelength of the interior convection rolls is consistently too large compared to theory. We tentatively attribute this observation to wavelength forcing effects associated with the periodic structure of the packing.

In the present study, we examined five specific predictions based on the assumption of homogeneous Darcian flow. Four of these – the pattern at onset, the wavenumber at onset, the stability of patterns in the predicted region of stability, and the type of patterns produced after secondary instabilities occur – can only be examined in a system which can be visualized. The fifth prediction, the slope of *Nu* versus *Ra*, has been examined before, but we included it for completeness. Of five predictions based on continuum theory, we find that two, the qualitative pattern at onset (rolls) and the size of the stability region (at least near the observed critical wavevector), match experiment. Specifically, we found stable roll-like states near onset which remained stable up to $\epsilon = 5$. The states also relaxed rapidly, within $2\tau_v$–$5\tau_v$, after quenching from a time-dependent state at $\epsilon = 7$. This is consistent with (although not a direct proof of) the rapid decay of vertical vorticity. The wavenumber at onset, the secondary

instabilities, and the *Nu* versus *Ra* curve do not agree with theory. We measure the wavenumber at onset to be 0.7π instead of π. The stable time-independent states are predicted to lose stability to time-independent cross-roll states. Instead we find that they lose stability to a time-dependent cellular state, possibly with hexagonal symmetry. The measured slope of the *Nu* versus *Ra* curve, 0.73 ± 0.05, differs from the prediction of 2. We have also observed an interesting asymmetry in the size of the upflowing and downflowing rolls. The ratio of the width of the upflowing rolls to that of the downflowing rolls tends to decrease as ϵ is increased. As ϵ is increased further the upflowing rolls become isolated islands or plumes of upflow in a large background of downflow. The result is a time-dependent state starting at $\epsilon \simeq 6$. A possible reason for this asymmetry is the variation of the fluid parameters across the layer height which occurs for large *Ra*.

The present experiments indicate that new theories of PMC should include information on the pore structure. Alternatively, experiments on different media which are not constructed from sphere packings may provide new and useful information. In that vein, studies of convection for binary mixtures, where travelling wave states are expected for homogeneous media, may provide an effective testing ground for theories of porous flow.

This work was supported by the US DOE, Office of Basic Energy Sciences, Grant DE-FG05-90R14141 and (G.A.J.) by NIH grant No. P41 RR05959.

REFERENCES

Ashcroft, N. W. & Mermin, N. D. 1976 *Solid State Physics*. Fort Worth: Saunders.

Bear, J. 1988 *Dynamics of Fluids in Porous Media*. Dover.

Beckermann, C., Viskanta, R. & Ramadhyani, S. 1988 Natural convection in vertical enclosuers containing simultaneously fluid and porous layers. *J. Fluid Mech.* **186**, 257–284.

Behringer, R. P. 1985 Rayleigh-Bénard convection and turbulence in liquid helium. *Rev. Mod. Phys.* **57**, 657–687.

Bloch, F. 1946 Nuclear induction. *Phys. Rev.* **70**, 460–474.

Bodenschatz, E., Bruyn, J. de, Ahlers, G. & Cannell, D. S. 1991 Transitions between patterns in thermal convection. *Phys. Rev. Lett.* **67**, 3078–3081.

Bories, S. & Thirriot, C. 1969 E'changes thermiques et tourbillons dans une couche poreuse horizontale. *La Houille Blanche* **24**, 237–245.

Boussinesq, J. 1903 *Théorie Analytique de la Chaleur*, vol. 2. Gauthier-Villars.

Bruyn, J. de, Bodenschatz, E., Morris, S. W., Trainoff, S. P., Hu, Y., Cannell. D. S. & Ahlers, G. 1996 Apparatus for the study of Rayleigh-Bénard convection in gas under pressure. *Rev. Sci. Instrum.* **67**, 2043–2067.

Buretta, R. J. & Berman, A. S. 1976 Convective heat transfer in a liquid saturated porous layer. *Trans. ASME J. Appl. Mech.* **43**, 249–253.

Busse, F. H. 1967 The stability of finite amplitude cellular convection and its relation to an extremum principle. *J. Fluid Mech.* **30**, 625–649.

Busse, F. H. 1985 Transition to turbulence in Rayleigh-Bénard convection. In *Hydrodynamic Instabilities and the Transition to Turbulence*, 2nd edn (ed. H. L. Swinney & J. Gollub), pp. 97–137. Springer.

Busse, F. H. & Joseph, D. D. 1972 Bounds for heat transport in a porous layer. *J. Fluid Mech.* **54**, 521–543.

Busse, F. H. & Whitehead, J. A. 1971 Instabilities of convection rolls in a high Prandtl number fluid. *J. Fluid Mech.* **47**, 305–320.

Callaghan, P. T. *Principles of Nuclear Magnetic Resonance Microscopy*. Clarendon.

Close, D. J., Symons, J. G. & White, R. F. 1985 Convective heat tranfer in shallow gas-filled porous media. *Intl J. Heat Mass Transfer* **28**, 2371–2378.

Combarnous, M. 1970 Convection naturelle et convection mixte dans une couche poreuse horizontale. *Rev. Gén. Therm.* **9**, 1355–1375.

Combarnous, M. & Bories, S. A. 1975 Hydrothermal convection in saturated porous media. *Hydroscience* **10**, 231–307.

Cross, M. C. & Hohenberg, P. C. 1993 Pattern formation outside of equilibrium. *Rev. Mod. Phys.* **65**, 851–1112.

Darcy, H. 1856 *Les Fontaines Publiques de la Ville de Dijon.* Dalmont.

Dullien, F. A. L. 1979 *Porous Media: Fluid Transport and Pore Structure.* Academic.

Dumoulin, C. L. 1986 Magnetic resonance angiography. *Radiology* **161**, 717–720.

Elder, J. W. Steady free convection in a porous medium heated from below. *J. Fluid Mech.* **27**, 29–48.

Ene, H. I. & Poliševski, D. 1987 *Thermal Flow in Porous Media.* Reidel.

Ergun, S. 1952 Fluid flow through packed columns. *Chem. Engng Prog.* **48**, 89–94.

Georgiadis, J. G. 1991 Future research needs in convective heat and mass transport in porous media. In *Convective Heat and Mass Transfer* (ed. S. Kakac, B. Kilkis, F. A. Kulacki & F. Arinc). NATO ASI Series E, vol. 196, pp. 1073–1088. Kluwer.

Georgiadis, J. G., Behringer, R. P., Shattuck, M. D. & Johnson, G. A. 1991 Interstitial velocity and temperature fields in fully-saturated porous media. In *Proc. 9th Symp. on Energy Sciences.* US Department of Energy.

Givler, R. C. & Altobelli, S. A. 1994 A determination of the effective viscosity for the Brinkman-Forchheimer flow model. *J. Fluid Mech.* **258**, 355–370.

Greenside, H. S., Cross, M. C. & Coughran, W. M. 1988 Mean flows and the onset of chaos in large-cell convection. *Phys. Rev. Lett.* **60**, 2269–2272.

Gupta, V. P. & Joseph, D. D. 1973 Bounds for heat transport in a porous layer. *J. Fluid Mech.* **57**, 491–514.

Horton, C. W. & Rodgers, F. T. 1945 Convection currents in a porous media. *J. Appl. Phys.* **16**, 367–370.

Howle, L. E., Behringer, R. P. & Georgiadis, J. G. 1993*a* Shadowgraphic visualization of natural convection in rectangular-grid porous layers. In *Topics in Heat Transfer I* (ed. M. Keyhani *et al.*). HTD, vol. 206, pp. 230–232.

Howle, L. E., Behringer, R. P. & Georgiadis, J. G. 1993*b* Visualization of convective fluid flow in a porous medium. *Nature* **362**, 230–232.

Howle, L. E., Behringer, R. P. & Georgiadis, J. G. 1997 Convection in ordered and disordered porous media. Part 2. Visualization by shadowgraph. *J. Fluid Mech.* **332**, 247–262.

Joseph, D. D. 1976 *Stability of Fluid Motions, II.* Springer.

Kaneko, T., Mohtadi, M. F. & Aziz, K. 1974 An experimental study of natural convection in inclined porous media. *Intl J. Heat Mass Transfer* **17**, 485–496.

Katto, Y. & Masuoka, T. 1967 Criterion for the onset of convective flow in a fluid in a porous medium. *Intl J. Heat Mass Transfer* **10**, 297–309.

Kutsovsky, Y. E., Scriven, E., Davis, H. T. & Hammer, B. E. 1996 NMR image of velocity profiles and velocity distributions in bead packs. *Phys. Fluids* **8**, 863–871.

Lapwood, E. R. 1948 Convection of a fluid in a porous medium. *Proc. Camb. Phil. Soc.* **44**, 508–521.

Lebon, L., Oger, L., Leblond, J., Hulin, J. P., Martys, N. S. & Schwartz, L. M. 1996 Pulsed gradkiend NMR measurements and numerical simulation of flow velocity distribution in sphere packings. *Phys. Fluids* **8**, 293–301.

Lein, H. & Tankin, R. S. 1992 Natural convection in porous media – I. Nonfreezing. *Intl J. Heat Mass Transfer* **35**, 175–186.

Lister, C. R. B. 1990 An explanation for the multivalued heat transport found experimentally for convection in a porous medium. *J. Fluid Mech.* **214**, 287–320.

Martys, N. S., Torquato, T. & Benz, T. P. 1994 Universal scaling of fluid permeability for sphere packings. *Phys. Rev.* E **50**, 403–408.

Moran, P. R. 1982 A flow velocity zeugmatographic interlace for NMR imaging in humans. *Magnetic Resonance Imaging* **1**, 197–203.

Morris, S. W., Bodenschatz, E., Cannell, D. S. & Ahlers, G. 1993 Spiral defect chaos in large aspect ratio Rayleigh-Bénard convection. *Phys. Rev. Lett.* **71**, 2026–2029.

NEWELL, A. C., PASSOT, T. & LEGA, J. 1993 Order parameter equations for patterns. *Ann. Rev. Fluid Mech.* **25**, 399–453.

NEWELL, A. C. & WHITEHEAD, J. A. 1969 Finite bandwidth, finite amplitude convection. *J. Fluid Mech.* **38**, 279–303.

NIELD, D. A. & BEJAN, A. 1992 *Convection in Porous Media.* Springer.

OBERBECK, A. Ueber die Wärmeleitung der Flüssigkeiten bei Berücksichtigung der Strömungen infolge con Temperaturdifferenzen. *Ann. Phys. Chem.* **7**, 271–292.

O'DONNELL, M. 1985 NMR blood flow imaging using multiecho, phase contrast sequences. *Med. Phys.* **12**, 59–64.

PALM, E., WEBER, J. E. & KVERNVOLD, O. 1972 On steady convection in a porous medium. *J. Fluid Mech.* **54**, 153–161.

PRASAD, V., KULACKI, F. A. & KEYHANI, M. 1985 Natural convection in porous media. *J. Fluid Mech.* **150**, 89–119.

RASENAT, S., HARTUNG, G., WINKLER, B. L. & REHBERG, I. 1989 The shadowgraph method in convection experiments. *Exps. Fluids* **7**, 412–420.

REDPATH, T. W., NORRIS, D. G., JONES, R. A. & HUTCHISON, J. M. S. 1984 A new method of NMR flow imaging. *Phys. Med. Biol.* **29**, 891–898.

SCHNEIDER, K. J. 1963 Investigation on the influence of free thermal convection on the heat transfer through granular material. *Proc. 11th Intl Congr. of Refrigeration*, pp. 247–253. Pergamon.

SEGEL, L. A. 1969 Distant side-walls cause slow amplitude modulation of cellular convection. *J. Fluid Mech.* **38**, 203–224.

SHATTUCK, M. 1995 Flows in porous media: visualization by magnetic resonance imaging. Unpublished: Duke University.

SHATTUCK, M. D., BEHRINGER, R. P., JOHNSON, G. A. & GEORGIADIS, J. G. 1994 Magnetic resonance imaging of convection in porous media. In *Proc. 12th Symp. on Energy Sciences.*

SHATTUCK, M. D., BEHRINGER, R. P., JOHNSON, G. A. & GEORGIADIS, J. G. 1995 Onset and stability of convection in porous media: visualization by magnetic resonsnce imaging. *Phys. Rev. Lett.* **75**, 1934–1937.

SIGGIA, E. D. & ZIPPELIUS, A. 1981 Pattern selection in Rayleigh-Bénard convection near threshold. *Phys. Rev. Lett.* **47**, 835–838.

SINGER, J. R. 1980 Blood flow measurements by NMR of the intact body. *IEEE Trans. Nuclear Sci.* **27**, 1245–1249.

SLICHTER, C. P. 1978 *Principles of Magnetic Resonance.* Springer.

STRAUS, J. M. 1974 Large amplitude convection in porous media. *J. Fluid Mech.* **64**, 51–63.

TORRANCE, K. E., SCHOENHALS, R. J., TIEN, C. L. & VISKANTA, R. 1982 Natural convection in porous media. In *Proc. Workshop on Natural Convection* (ed. K. T. Yang & J. R. Lloyd), pp. 36–45. University of Notre Dame, Indiana.

WHITAKER, S. 1986 Flow in porous media: a theoretical derivation of Darcy's law. *Transport in Porous Media* **1**, 3–25.

XI, H.-W., GUNTON, J. D. & VINALS, J. 1993 Spiral defect chaos in a model of Rayleigh-Bénard convection. *Phys. Rev. Lett.* **71**, 2030–2033.

YEN, Y. C. 1974 Effects of density inversion on free convective heat transfer in porous layer heated from below. *Intl J. Heat. Mass Transfer* **17**, 1349–1356.

ZIMMERMANN, W., SESSELBERG, M. & PETRUCCIONE, F. 1993 Effect of disorder in pattern formation. *Phys. Rev.* E **71**, 2699–2703.